Toward Segmentation of 3D Probability Density Fields by Surface Evolution: Application to Diffusion MRI

Christophe Lenglet, Mikaël Rousson, Rachid Deriche, Olivier Faugeras

INSTITUT NATIONAL DE RECHERCHE EN INFORMATIQUE ET EN AUTOMATIQUE

Toward Segmentation of 3D Probability Density Fields by Surface Evolution: Application to Diffusion MRI

Christophe Lenglet — Mikaël Rousson — Rachid Deriche — Olivier Faugeras

N° 5243

June, 2004

Thème BIO

ISSN 0249-6399

Toward Segmentation of 3D Probability Density Fields by Surface Evolution: Application to Diffusion MRI

Christophe Lenglet* , Mikaël Rousson† , Rachid Deriche‡ , Olivier Faugeras§

Thème BIO — Systèmes biologiques
Projet Odyssée

Rapport de recherche n° 5243 — June, 2004 — 27 pages

Abstract: We propose three original approaches for the segmentation of three-dimensional fields of probability density functions. This presents a wide range of applications in medical image processing, in particular for diffusion magnetic resonance imaging where each voxel is assigned with a function describing the average motion of water molecules. Being able to automatically extract relevant anatomical structures of the white matter, such as the *corpus callosum*, would dramatically improve our current knowledge of the cerebral connectivity as well as allow for their statistical analysis. Our first approach involves the use of a multivariate Gaussian law to approximate the distribution of the components of diffusion tensors for each sub-region of a DTI volume. The second technique relies on the use of the symmetrized Kullback-Leibler distance and on the modelization of its distribution over the subsets of interest in the volume. The third technique considers the 6-dimensional statistical manifold defined by the parameters of the diffusion tensors and proposes a segmentation algorithm by rigorously defining the geodesic distance and the intrinsic mean on this Riemannian manifold. The variational formulations of the problems yield three differents level-set evolutions converging towards the respective optimal segmentation. We validate these approaches on synthetical data and show promising results on the extraction of the *corpus callosum* and of the lateral brain ventricles from a real dataset.

Key-words: Segmentation, Diffusion Tensor Imaging, Kullback-Leibler Divergence, Information Geometry, Riemannian Geometry, Level-Set.

* Christophe.Lenglet@sophia.inria.fr
† Mikaël.Rousson@sophia.inria.fr
‡ Rachid.Deriche@sophia.inria.fr
§ Olivier.Faugeras@sophia.inria.fr

Unité de recherche INRIA Sophia Antipolis
2004, route des Lucioles, BP 93, 06902 Sophia Antipolis Cedex (France)
Téléphone : +33 4 92 38 77 77 —Télécopie : +33 4 92 38 77 65

Segmentation d'un champ de densités de probabilités 3D par évolution de surface: application à l'IRM de diffusion

Résumé : Nous proposons trois approches originales pour la segmentation d'un champ de densités de probabilités 3D. Ce travail a de nombreuses applications en imagerie médicale, en particulier pour les images de diffusion à résonance magnétique où une fonction représentant le mouvement moyen des molécules d'eau est assignée à chaque voxel. L'extraction automatique de structures importantes dans la matière blanche, telles que le *corpus callosum*, pourrait permettre d'améliorer grandement notre connaissance des connectivités cérébrales. Dans la première approche, nous utilisons une loi Gaussienne multivariée afin d'approximer la distribution des composantes du tenseur de diffusion à l'intérieur de chaque sous région du volume DTI. La seconde technique est basée sur la version symétrisée de la distance de Kullback-Leibler et de la modélisation de sa distribution dans chaque région d'intéret. Dans la troisième approche, nous considérons la variété statistique de dimension 6 définie par les paramètres du tenseur de diffusion et nous proposons un nouvel algorithme en définissant distance géodésique et moyenne intrinsèque dans cette variété Riemannienne. Les formulations variationelles du problème conduisent à trois évolutions différentes sur des ensembles de niveaux qui convergent vers la segmentation optimale correspondante. Nous validons ces approches sur des données synthétiques et nous montrons des résultats prometteurs pour l'extraction du *corpus callsoum* et des ventricules latéraux.

Mots-clés : Segmentation, images de tenseurs de diffusion, divergence de Kullback-Leibler, géométrie de l'information, géométrie Riemannienne, ensembles de niveaux.

Contents

1 Introduction

Diffusion magnetic resonance imaging is a relatively new modality [5], [25] able to quantify the anisotropic diffusion of water molecules in highly structured biological tissues. In 1994, P. Basser [2] proposed to model voxelwise the probability density function of the molecular motion $r \in \mathbb{R}^3$ by a Gaussian law whose covariance matrix is given by the diffusion tensor $\mathbf{D}$. Diffusion Tensor Imaging (DTI) then produces a volumic image containing, at each voxel, a 3×3 symmetric positive-definite tensor. The estimation of these tensors requires the acquisition of diffusion weighted images in different sampling directions together with a T2 image. Numerous algorithms have been proposed to perform a robust estimation and regularization of these tensors fields [45], [51]. Recently, Q-ball Imaging has been introduced by D. Tuch et al. [47] in order to reconstruct the Orientation Distribution Function (ODF) by the Funk-Radon transform of high b-factor diffusion weighted images acquired under the narrow pulse approximation. This ODF is the symmetric probability density function $S^2 \rightarrow \mathbb{R}$ giving the probability for a spin to diffuse in a given direction. This method provides a better angular constrast and is able to recover intra-voxel fiber crossings.
Diffusion MRI is particularly relevant to a wide range of clinical pathologies investigations such as acute brain ischemia detection [43], stroke, Alzheimer disease, schizophrenia [1] ...etc. It is also extremely useful in order to identify the neural connectivity of the human brain [21], [48], [9]. As of today, diffusion MRI is the only non-invasive method that allows us to distinguish the various anatomical structures of the cerebral white matter such as the *corpus callosum*, the *arcuate fasciculus* or the *corona radiata*. These are examples of commisural, associative and projective neural pathways, the three major types of fiber bundles, respectively connecting the two hemispheres, regions of a given hemisphere or the cerebral cortex with subcortical areas. In the past, many techniques have been proposed to classify gray matter, white matter and cephlo-spinal fluid from T1-weighted MR [54] images but the literature addressing the issue of white matter internal structures segmentation is just beginning [56], [17], [50], [49] and [53].
In the following, we first address the segmentation of cerebral structures on the basis of statistics over the field of diffusion tensors components, thus exploiting the entire information encapsulated by this Gaussian descriptor. We then introduce another original technique for the segmentation of any probability density function (*pdf*) field by examining the statistics of the distribution of the Kullback-Leibler distances between theses *pdfs*. We finally propose a novel method based on the representation of the family of Gaussian probability density functions by a 6-dimensional statistical differential manifold $\mathcal{M}$. Our goal is to perform the direct segmentation of internal structures of the white matter. Zhukov et al. [56] defined an invariant anisotropy measure in order to drive the evolution of a level-set and isolate strongly anisotropic regions of the brain. The reduction of the full tensor to a single scalar gives a relatively low discrimination power to the method potentially resulting in segmentation of mixed structures. On the other side, Wiegell et al. [53], Jonassan et al. [17] and Wang et al. [49], [50] proposed different measures of dissimilarity between full diffusion tensors: The first and last methods use the Frobenius norm of the difference of tensors, together with a spatial coherence or regularity term respectively in a k-means algorithm or active

contour model to perform the segmentation of the thalamus nuclei. In [53], the nature of the elements to be segmented (compact, homogeneous) verify the restrictive hypothesis of the technique, which is rarely the case. In [49], the segmentation is restricted to the 2D case. The second method introduces a geometric measure of dissimilarity by computing the normalized tensor scalar product of two tensors, which is nothing but a measure of overlap. Finally, the third method relies on the natural distance between two Gaussian *pdfs*, given by the symmetrized Kullback-Leibler distance, elegantly derives an affine invariant dissimilarity measure between diffusion tensors and applies it to the segmentation of 2D fields of *pdfs*. We will first aim to take advantage of the statistical information like the covariance of the diffusion tensor components to refine the segmentation process and hence recover irregular anatomical structures such as the minor and major forceps of the *corpus callosum*. This first approach was published in [40]. We then generalize the method proposed in [49] to the 3D case [22] and propose to fit the distribution of the symmetrized Kullback-Leibler (KL) distances by a Gaussian law. KL distances are taken between any *pdf* and our method is thus applicable not only to DTI but also to Q-ball data which should enable the proposed algorithm to catch even finer details. At last, taking into account the Riemannian geometry of the space of Gaussian *pdfs* will allow us to precise the notion of intrinsic Gaussian law between Gaussian *pdfs* in order to improve our segmentation algorithm. Section 2 will recall basic notions related to diffusion MRI and white matter connectivity mapping. Section 3 will detail our technique for tensor fields segmentation based on the statistics of tensorial components. Section 4 will expose our method for a general algorithm of probability density fields segmentation together with its application to the Gaussian case. Section 5 will recall basic notions on the Fisher information matrix and the geodesic distance and the intrinsic mean on the underlying manifold are considered to define a new segmentation algorithm. Section 6 will present and discuss experimental results both on synthetic and real DTI datasets.

2 From Diffusion Weighted MRI to Fiber Tracking

In the following, we describe the method used for the acquisition of our data and the robust estimation of the diffusion tensor. We briefly review classical tractography algorithms since we will use their result to illustrate in Fig.7 the accuracy of our segmentation algorithm.

2.1 Data Acquisition, DTI

Our dataset consists of 30 diffusion weighted images $S_k : \Omega \to \mathbb{R},\ k = 1, ..., 30$ as well as 1 image S_0 corresponding to the signal intensity in the absence of a diffusion-sensitizing field gradient (ie. $b = 0$ in equation 1). They were obtained on a GE $1.5\ T$ Signa Echospeed with standard 22 mT/m gradient field. The echoplanar images were acquired on 56 evenly spaced axial planes with a 128×128 pixels in each slice. Voxel size is $1.875\ mm \times 1.875\ mm \times 2.8\ mm$. 6 gradient directions $\mathbf{g}_k$, each with 5 different b-factors and 4 repetitions were used. Imaging parameters were: b values between 0 and 1000 $s.mm^{-2}$, $TR = 2.5\ s$, $TE = 84.4\ ms$ and a

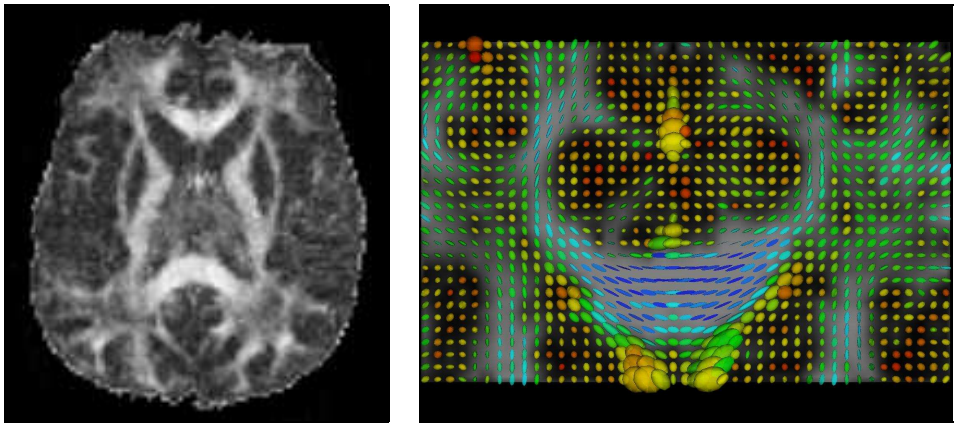

Figure 1: [left] Fractional Anisotropy map and [right] Corresponding tensors in the genu of the corpus callosum

square field of view of 24 cm [37]. We recall that the estimation of a field of 3×3 symmetric positive definite tensors $\mathbf{T}$ is done by using the Stejskal-Tanner equation [44] for anisotropic diffusion 1 at each voxel x.

$$S_k(x) = S_0(x) e^{-b\mathbf{g}_k^T \mathbf{T}(x) \mathbf{g}_k} \quad \forall x \in \Omega \tag{1}$$

where $\mathbf{g}_k$ are the normalized non-collinear sensitizing gradient and b the diffusion weighting factor. Various methods have been proposed for the estimation of the 6 elements of $\mathbf{T}(x)$ by using equation 1 (see figure 1). A survey of these approaches and a variational framework for the estimation and the regularization of of DTI data can be found in [45]. This last method provides a convenient mean to impose important constraints on the sought solution such as tensor positivity, orthonormality of the eigenvectors or some degree of smoothness of the result. This is performed by minimizing the following energy on the manifold of positive definite tensors $P(3)$:

$$\underset{\mathbf{T} \in P(3)}{\text{Arg min}} \int_\Omega \sum_{k=1}^{n} \psi(\| \ln(S_0/S_k) - b\mathbf{g}_k^T \mathbf{T} \mathbf{g}_k \|) + \alpha \rho(\|\nabla \mathbf{T}\|) d\Omega \tag{2}$$

2.2 Fiber Tracking

The main idea on which relies classical tractography [29], [28], [37], [55] is that, despite the potentially multi-directional environment within a voxel, water diffusion in many regions of the white matter is highly anisotropic and consequently the orientation of the largest tensor eigenvector aligns with predominant axonal orientation [30]. It should be safe to

say that, accepting this restrictive assumption will enable us to identify macroscopical 3D architectures of the white matter. This gives rise to the line propagation technique that we have implemented and tested with various possible approaches. However, these local methods incorporate strong limitations and refinements have been proposed [3], [19], [20], [24], [46], [52], [9], [48]. More global algorithms [21], [31], [33], [35], [12], stochastic modeling [6], [34], [16] or new acquisition methods were also introduced to try to overcome that restriction. The section dedicated to the experimental results will make use of the method proposed by the authors in [21] in order to assess the accuracy of the segmentation process with regard to the structure of the axonal fibers in the *corpus callosum*.

3 Diffusion Tensor Images Segmentation

As shown in the previous section, the diffusion tensor is directly related to tissue properties. Then, classical segmentation techniques can be applied on this type of images for the extraction of white matter structures of particular interest. The level set representation is a well-suited framework for curve/surface evolution. Let Γ be the optimal boundary between the 3D object to extract Ω_1 and the 3D background Ω_2, we introduce the level set function $\phi : \Omega \rightarrow \mathbb{R}^3$, defined as follow:

$$\begin{cases} \phi(x) = 0, & \text{if } x \in \Gamma \\ \phi(x) = \mathcal{D}(x,\Gamma), & \text{if } x \in \Omega_1 \\ \phi(x) = -\mathcal{D}(x,\Gamma), & \text{if } x \in \Omega_2 \end{cases} \tag{3}$$

where $\mathcal{D}(x,\Gamma)$ stands for the Euclidean distance between x and Γ and $\Omega = \Omega_1 \cup \Omega_2$. Furthermore, let $H_\epsilon(z)$ and $\delta_\epsilon(z)$ be regularized versions of the Heaviside and Dirac functions as defined in [10].

Let p_1 and p_2 be the probability density functions of the diffusion tensor inside and outside Γ. Then, according to the Geodesic Active Regions model [32], the object can be recovered by minimizing:

$$E(\phi) = -\int_\Omega \Big(H_\epsilon(\phi) \log p_1(T(x)) + (1 - H_\epsilon(\phi)) \log p_2(T(x)) \Big) dx \tag{4}$$

The direct definition of a probability density function in the space of symmetric positive definite matrix is a difficult problem and thus, we will rather consider vector representations of the tensors in $\mathbb{R}^6$. By analogy to the information geometry approach, we consider a statistical distribution on linear spaces which overcome the hypothesis of isotropic distribution. Hence, as done in [41] for texture images with the structure tensor, we consider a parametric approximation with a 6D Gaussian. Let u be the vector representation of a tensor T, the likelihood of u in the region X is given by:

$$p_X(u|\mu_X, \Sigma_X) = \frac{1}{(2\pi)^3 |\Sigma_X|^{1/2}} e^{-\frac{1}{2}(u-\mu_X)^T \Sigma_X^{-1} (u-\mu_X)} \tag{5}$$

By construction, the diagonal and non-diagonal components of a diffusion tensor are highly correlated and so, a full covariance must be considered in the density of its vector representation u. Then, the vector means and the covariances of these densities are also supposed unknown. However, these parameters can be introduced as unknown in (4). If we also add a regularity constraint on the interface, we obtain the final objective function:

$$\begin{aligned} E(\phi, \{\mu_X, \Sigma_X\}) = \nu \int_\Omega |\nabla H_\epsilon(\phi)| d\mathbf{x} \\ - \int_\Omega H_\epsilon(\phi) \log p_1(u(\mathbf{x})|\mu_1, \Sigma_1) dx \\ - \int_\Omega (1 - H_\epsilon(\phi)) \log p_2(u(\mathbf{x})|\mu_2, \Sigma_2) dx \end{aligned} \tag{6}$$

This type of energy was studied in [39], the Euler Lagrange equation for ϕ yields the following evolution equation for the Level Set function:

$$\begin{aligned} \phi_t(x) = \delta_\epsilon(\phi(x)) \Big(\nu \, \mathrm{div} \frac{\nabla \phi}{|\nabla \phi|} + \frac{1}{2} \log \frac{|\Sigma_2|}{|\Sigma_1|} \\ - \frac{1}{2} (u(x) - \mu_1)^T \Sigma_1^{-1} (u(x) - \mu_1) \\ + \frac{1}{2} (u(x) - \mu_2)^T \Sigma_2^{-1} (u(x) - \mu_2) \Big) \quad \forall x \in \mathbb{R}^3 \end{aligned} \tag{7}$$

while the statistical parameters are updated with:

$$\begin{aligned} \mu_1(\phi) &= \frac{\int_\Omega u(x) H_\epsilon(\phi) dx}{\int_\Omega H_\epsilon(\phi) dx} \\ \mu_2(\phi) &= \frac{\int_\Omega u(x)(1 - H_\epsilon(\phi)) dx}{\int_\Omega (1 - H_\epsilon(\phi)) dx} \\ \Sigma_1(\phi) &= \frac{\int_\Omega (\mu_1 - u(x))(\mu_1 - u(x))^T H_\epsilon(\phi) dx}{\int_\Omega H_\epsilon(\phi) dx} \\ \Sigma_2(\phi) &= \frac{\int_\Omega (\mu_2 - u(x))(\mu_2 - u(x))^T (1 - H_\epsilon(\phi)) dx}{\int_\Omega (1 - H_\epsilon(\phi)) dx} \end{aligned} \tag{8}$$

Adequate implementation schemes for this type of optimization can be found in [10]. Two important details must be noted: (i) the explicit scheme is not stable for any time step because of regularization term, (ii) the level set function is reinitialized to the distance function at each iteration. If we restrict the covariance matrix to the identity matrix, these equations simplify and the log-likelihoods in Eq.(4) become simply the Euclidean distance between the vectors u and μ_X, which is equivalent to the Frobenius norm of the difference between the corresponding tensors, as nicely studied in [49].

4 Probability Density Fields Segmentation

4.1 General case

Let $p(x,r)$ be the probability density function of our random vector r of $\mathbb{R}^3$ describing the water molecules average motion at a given voxel x of a diffusion MR image $\Omega \subset \mathbb{R}^3$ and for a given diffusion time τ imposed by the parameters of the PGSE (Pulsed Gradient Spin Echo) sequence. We are interested in characterizing the global coherence of that *pdf* field and use the classical symmetrized Kullback-Leibler distance to that end. With $p(x), q(y)\ \forall x, y \in \Omega$ two *pdfs* from $\mathbb{R}^3$ onto $\mathbb{R}^+$, their KL distance is given by

$$d(p,q) = KL(p,q) = \frac{1}{2}\int_{\mathbb{R}^3}\left(p(r)\log\frac{p(r)}{q(r)} + q(r)\log\frac{q(r)}{p(r)}\right)dr \tag{9}$$

Assuming a partition of the data between the structure we try to segment Ω_1 and the rest of the volume Ω_2, we again seek the optimal separating surface Γ between those two subsets. We denote by $\overline{p}_1$ and $\overline{p}_2$ the most representative *pdfs* over Ω_1 and Ω_2 verifying equation 13. It is then possible to model the distribution of the KL distances to $\overline{p}_1$ and $\overline{p}_2$ in their respective domains by suitable densities $p_{d,1}, p_{d,2}$. In the following, we make the assumption that $p_{d,1}, p_{d,2}$ are Gaussian of zero mean and variances σ_1^2, σ_2^2. It is indeed natural to impose the mean distance to the *pdfs* $\overline{p}_1$ and $\overline{p}_2$ to be as small as possible, while retaining an important degree of freedom by considering the variances of those distributions.
We then define the following energy in order to maximize the likelihood of these densities on their associated domain:

$$E(\Omega_i, \sigma_i^2, \overline{p}_i) = \sum_{i=1}^{2}\int_{\Omega_i} -\log p_{d,i}(d(p(x), \overline{p}_i))dx \tag{10}$$

where

$$p_{d,i} = \frac{1}{\sqrt{2\pi\sigma_i^2}}\exp\frac{-d^2(p,\overline{p}_i)}{2\sigma_i^2}$$

Of course, other models can easily be used for the $p_{d,i}$. Note that in the case where the σ_i are equal to 1, this energy will equal to the one proposed in [50]. In the experimental part, the importance of adding σ_i will be illustrated. We can now rewrite equation 10 and introduce a regularity constraint on Γ as follows:

$$\int_\Omega -\log p_{d,1}(d(p(x),\overline{p}_1))H(\phi) - \log p_{d,2}(d(p(x),\overline{p}_2))(1-H(\phi)) + \nu|\nabla H_\epsilon(\phi)|dx \tag{11}$$

The derivation of the Euler-Lagrange equations for this class of energy was studied in [39] and yields the following evolution for ϕ:

$$\phi_t(x) = \delta_\epsilon(\phi(x))\left(\nu\mathrm{div}\frac{\nabla\phi}{|\nabla\phi|} + \frac{1}{2}\log\frac{p_{d,2}}{p_{d,1}}\right)\ \forall x \in \Omega \tag{12}$$

Moreover, the derivation of the energy with respect to σ_i^2 and $\overline{p}_i$ provide the update formulae for these statistical parameters. It can be shown that the variance must be updated with its empirical estimation (see equation 8) whereas some more work is needed for the $\overline{p}_i$. We indeed have to estimate:

$$\tilde{p}_i = argmin \int_{\Omega_i} KL^2(\overline{p}_i, p(x))dx \tag{13}$$

For a general *pdf* $p(x)$, for instance if we consider the ODF derived from Q-ball data, the variance is easily computed as in [39] but the estimation of the $\tilde{p}_i$ might require the use of numerical approximation techniques if no closed-form is available.

4.2 Application to Gaussian Distributions

We now explicitely express the energy 10 for Gaussian *pdf*s and use a zero-mean Gaussian law to model the distribution of their distances. The energy becomes

$$\begin{aligned} E(\Omega_i, \sigma_i^2, \overline{p}_i) = \int_\Omega \frac{1}{2}\Big(& \big(\log(2\pi\sigma_1^2) + d^2(p(x), \overline{p}_1)\sigma_1^{-2}\big)H(\phi) \\ & + \big(\log(2\pi\sigma_2^2) + d^2(p(x), \overline{p}_2)\sigma_2^{-2}\big)(1 - H(\phi))\Big) \\ & + \nu|\nabla H_\epsilon(\phi)|dx \end{aligned}$$

If we write, as in [50], the Kullback-Leibler distance between two Gaussian *pdf*s parametrized by their covariance matrices (*.ie* the Diffusion Tensor $\mathbf{D}$) as:

$$d^2(p(x), \overline{p}_i) = \frac{1}{2}\left(\text{trace}\left[\mathbf{D}^{-1}(x)\overline{\mathbf{D}}_i + \overline{\mathbf{D}}_i^{-1}\mathbf{D}(x)\right] - 3\right) \tag{14}$$

then the Euler-Lagrange equations for our energy become:

$$\begin{aligned} \phi_t(x) = \delta_\epsilon(\phi(x))\Big(\nu \text{div}\frac{\nabla\phi}{|\nabla\phi|} + \frac{1}{2}\Big(\log\frac{\sigma_2}{\sigma_1} + \frac{1}{4}\Big(\text{trace}\Big[\mathbf{D}^{-1}(x)\overline{\mathbf{D}}_2 + \overline{\mathbf{D}}_2^{-1}\mathbf{D}(x)\Big]\sigma_2^{-2} - \\ \text{trace}\Big[\mathbf{D}^{-1}(x)\overline{\mathbf{D}}_1 + \overline{\mathbf{D}}_1^{-1}\mathbf{D}(x)\Big]\sigma_1^{-2}\Big) + \\ \frac{3(\sigma_1^2 - \sigma_2^2)}{2(\sigma_1^2\sigma_2^2)}\Big)\Big) \ \forall x \in \Omega \end{aligned} \tag{15}$$

Notice that we obtain additional terms (the σ_i coefficients) in 15 if compared to the Euler-Lagrange equations proposed in [50]. For a given state of ϕ, closed-forms for the optimal covariance matrices of each region are available. In their recent paper, Wang et al. [50] nicely showed that these covariance matrices are given by

$$\tilde{\mathbf{D}}_i = \sqrt{\mathbf{B}_i^{-1}}\left(\sqrt{\sqrt{\mathbf{B}_i}\mathbf{A}_i\sqrt{\mathbf{B}_i}}\right)\sqrt{\mathbf{B}_i^{-1}}$$

where

$$\mathbf{A}_i = \int_{\Omega_i} \mathbf{D}(x)dx \quad \text{and} \quad \mathbf{B}_i = \int_{\Omega_i} \mathbf{D}^{-1}(x)dx$$

thus giving the update formula of the $\tilde{p}_i$.

5 Segmentation on the Statistical Manifold

We now consider the statistical manifold $\mathcal{M}$ representing the family of three-dimensional Gaussian probability density functions through the 6 parameters of their covariance matrix. The *pdf*s are, again, assumed to be of 0-mean since this simply translates the fact that the average displacement of spins in a voxel is zero. Following the work by Rao [38], where a Riemannian metric was introduced in term of the elements of the information matrix, we wish to define geodesic distances and intrinsic means on this 6-dimensional manifold whose coordinate system is given by a real vector parameter $\Theta = (\theta_1, ..., \theta_6) \in \mathbb{R}^6$ such that for all random vector $r \in \mathbb{R}^3$, $\mathcal{M} = \{p(r|\Theta\}$. In the following, we first show the main technical limitation of the Kullback-Leibler divergence together with its impact on the segmentation process. Then, we present the closed-form of the geodesic distance as well as the intrinsic mean which can be estimated for multivariate Gaussian densities with common mean.

5.1 The Fisher Information Matrix

The information manifold $(\mathcal{M}, g)$ equipped with the Fisher information matrix $g_{ij} = G$ has the structure of a Riemannian manifold [38] when G is non-degenerate. We recall that G is defined as follows:

$$g_{ij} = \mathbb{E}\left[\frac{\partial \log p(r,\Theta)}{\partial \theta_i} \frac{\partial \log p(r,\Theta)}{\partial \theta_j}\right] = \int_{\mathbb{R}^3} \frac{\partial \log p(r,\Theta)}{\partial \theta_i} \frac{\partial \log p(r,\Theta)}{\partial \theta_j} p(r,\Theta)dr \qquad (16)$$

Chentsov [11] proved in 1972 that G was the only metric satisfying certain invariant affine connections in the manifold of probability distributions. By plugging the definition of a Gaussian distribution into equation 16, the 6×6 metric tensor, as presented in [23], can be expressed in terms of the parameters $\theta_i,\ i = 1, ..., 6$ used to describe the *pdf*s.

Examples: **1.** If the diffusion process is locally isotropic (ie. if its covariance matrix $\mathbf{D}$ is the identity), the Fisher information matrix reduces to:

$$\begin{bmatrix} 1/2 & 0 & 0 & 0 & 0 & 0 \\ 0 & 1 & 0 & 0 & 0 & 0 \\ 0 & 0 & 1 & 0 & 0 & 0 \\ 0 & 0 & 0 & 1/2 & 0 & 0 \\ 0 & 0 & 0 & 0 & 1 & 0 \\ 0 & 0 & 0 & 0 & 0 & 1/2 \end{bmatrix} \qquad (17)$$

2. In the more general case of an anisotropic diffusion of variances $\sigma_1^2, \sigma_2^2, \sigma_3^2$ whose principal axis coincide with the coordinate frame of the image, the metric writes:

$$\begin{bmatrix} \frac{1}{2\sigma_1^4} & 0 & 0 & 0 & 0 & 0 \\ 0 & \frac{1}{\sigma_1^2\sigma_2^2} & 0 & 0 & 0 & 0 \\ 0 & 0 & \frac{1}{\sigma_1^2\sigma_3^2} & 0 & 0 & 0 \\ 0 & 0 & 0 & \frac{1}{2\sigma_2^4} & 0 & 0 \\ 0 & 0 & 0 & 0 & \frac{1}{\sigma_2^2\sigma_3^2} & 0 \\ 0 & 0 & 0 & 0 & 0 & \frac{1}{2\sigma_3^4} \end{bmatrix} \tag{18}$$

These simple examples make it obvious that the second, third and fifth diagonal terms of the metric G receive contributions from cross-terms between the diagonal elements of the covariance matrices described by the $\theta_i,\ i = 1, 4, 6$. Hence the factor $\frac{1}{2}$ in front of the first, fourth and sixth elements.
It becomes also clear now that, the approach developed in this section is an extension of the techniques described in section 3. Instead of considering the parametrized *pdf*s as living in the linear space $\mathbb{R}^6$, and thus taking $G = Id$, we do take into account the Riemannian structure of the underlying manifold through G.

The Kullback-Leibler divergence KLD (not its symmetrized form) turns out not only to yield a closed-form to evaluate the distance between two Gaussian densities but also to be a Taylor approximation of the geodesic distance between two nearby distributions $p(r, \Theta)$ and $p(r, \Theta + d\Theta)$. Indeed, we have:

$$KLD(\Theta, \Theta + d\Theta) = \int_{\mathbb{R}^3} p(r|\Theta) \log \frac{p(r|\Theta)}{p(r|\Theta + d\Theta)} dr$$

and by Taylor expansion with $d\Theta \to 0$

$$KLD(\Theta, \Theta + d\Theta) \sim \frac{1}{2} \sum_{ij} \mathbb{E}\left[- \frac{\partial^2 \log p(r|\Theta + d\Theta)}{\partial\Theta_i \partial\Theta_j} \right] d\Theta_i d\Theta_j$$

Noticing that

$$-\mathbb{E}\left[\frac{\partial^2 \log p(r|\Theta + d\Theta)}{\partial\Theta_i \partial\Theta_j} \right] = \mathbb{E}\left[\frac{\partial \log p(r, \Theta + d\Theta)}{\partial\theta_i} \frac{\partial \log p(r, \Theta + d\Theta)}{\partial\theta_j} \right]$$

makes it abvious that the square of the geodesic distance equals twice the KL divergence. We have to notice here that the geodesic distance is always defined with respect to a given element $p(r, \Theta)$ of $\mathcal{M}$ which yields its non-symmetric behavior. Moreover, we assume that we always compute distances between nearby elements of $\mathcal{M}$, which may not always hold. For general distributions, we may have no other choice but to consider this approximation.

However, in the more particular case of multivariate Gaussian densities with common means, a closed-form of the geodesic distance is available, avoiding any constraining limitation on comparable distributions. The next part introduced this geodesic distance and an algorithm for the estimation of the corresponding mean density is presented.

5.2 Geodesic Distance and Intrinsic Mean

We now concentrate on the space $S^+(m,\mathbb{R})$, endowed with the information metric ds^2. $S^+(m,\mathbb{R})$ denotes the set of $m \times m$ real symmetric positive-definite matrices. A detailed study on defining statistical models on this non-linear space was presented in [23]. Here we remind some important results, usefull for the segmentation task. Following [23] and [42, 7, 13, 8, 14, 26, 27], S^+ can be characterized as an affine symmetric space for which closed-form expressions are available for the solution of the geodesic equation as well as for the information geodesic distance (also known as Rao's distance). The information geodesic distance $\mathcal{D}$ between any two element Σ_1 and Σ_2 of S^+ is given by the theorem:

Theorem 5.1 (S.T. Jensen, 1976)
Consider the family of multivariate normal distributions with common mean vector ξ but differing variance-covariance matrices Σ. The geodesic distance between two members of the family with variance-covariance matrices Σ_1 and Σ_2 is given by

$$\mathcal{D}(\Sigma_1,\Sigma_2) = \frac{1}{2}\mathrm{tr}(\log^2(\Sigma_1^{-1/2}\Sigma_2\Sigma_1^{-1/2})) = \frac{1}{2}\sum_{i=1}^{m}\log^2(\lambda_i)$$

where the λ_i denote the m eigenvalues of the determinantal equation $|\lambda\Sigma_2 - \Sigma_1| = 0$.

Properties of the Geodesic Distance:
The distance $\mathcal{D}$ on S^+ defined above exhibits some nice properties that we hereafter summarize:

1. Positivity: $\mathcal{D}(\Sigma_1,\Sigma_2) \geq 0$, $\mathcal{D}(\Sigma_1,\Sigma_2) = 0 \Leftrightarrow \Sigma_1 = \Sigma_2$
2. Symmetry: $\mathcal{D}(\Sigma_1,\Sigma_2) = \mathcal{D}(\Sigma_2,\Sigma_1)$
3. Triangle inequality: $\mathcal{D}(\Sigma_1,\Sigma_3) \leq \mathcal{D}(\Sigma_1,\Sigma_2) + \mathcal{D}(\Sigma_2,\Sigma_3)$
4. Invariance under congruence transformations: $\mathcal{D}(\Sigma_1,\Sigma_2) = \mathcal{D}(P\Sigma_1P^T, P\Sigma_2P^T)$ $\forall P \in GL(m,\mathbb{R})$
5. Invariance under inversion: $\mathcal{D}(\Sigma_1,\Sigma_2) = \mathcal{D}(\Sigma_1^{-1},\Sigma_2^{-1})$

The interested reader can find more details about this in the technical report by Förstner and Moonen [14].

This natural distance can be used in the segmentation algorithm presented in the previous part, replacing the symetrized KL divergence by the new expression. For this purpose, we will need to estimate the empirical mean as proposed by Fréchet [15], Karcher [18] and Pennec [36]:

Definition 5.2 *The Normal distribution parametrized by* $\hat{\Sigma} \in S^+(m,\mathbb{R})$ *and defined as the empirical mean of* N *distributions* Σ_k, $k = 1, ..., N$, *achieves a local minimum of the function* $\mu : S^+(m,\mathbb{R}) \rightarrow \mathbb{R}^+$ *knwon as the empirical variance and defined as*

$$\mu(\Sigma_1, ..., \Sigma_N) = \frac{1}{N}\sum_{k=1}^{N} \mathcal{D}^2(\Sigma, \Sigma_k) = \mathbb{E}[\mathcal{D}^2(\Sigma, \Sigma_k)]$$

Karcher proved in [18] that such a mean, known as the Riemannian barycenter, exists and is unique for manifold of non-positive sectional curvature. This was shown to be the case for $S^+(m,\mathbb{R})$ in [23]. A closed-form of the mean cannot be obtained [27] but a gradient descent algorithm was proposed in [23]. A flow is derived from an initial guess $\hat{\Sigma}(0)$ toward the mean of a set of $S^+(m,\mathbb{R})$. The following evolution is obtained:

$$\partial_s \hat{\Sigma}(s) = -\frac{\hat{\Sigma}(s)}{N}\sum_{k=1}^{N} \mathrm{Log}(\Sigma_k^{-1}\hat{\Sigma}(s)) \tag{19}$$

The corresponding numerical implementation is detailed in [23].

Implementation: We can use the same variational framework as the one described in section 4 in order to maximize the likelihood of the approximate Normal densities on the Riemannian manifold. The energy is of the form 14 and the statistical parameters are updated by first, estimating the intrinsic mean in each region through the gradient descent 19, then computing the variances of the distance to these mean distributions.

6 Experimental Results and Comparisons

We will respectively refer to the methods presented in sections 3, 4 and 5 as Method 1, 2 and 3. We begin with a validation of Method 1 on synthetical data with "limit" cases where other approaches fail. Then, experiments are conducted on the extraction of the *corpus callosum* from real DTI data through Methods 1, 2 and 3. Moreover, we show how we can improve the robustness of our Method 2 by introducing an anisotropy measure. We exhibit promising results of Method 3. We finally present results on real data with fusion of segmentation and estimation of fibers in the *splenium* of the *corpus callosum*.

6.1 Synthetical data

Diffusion tensor images measure the displacement of water molecules. This displacement which characterize different tissues, can be splitted into two different information: its intensity and its direction. When considering diffusion tensor images, these information are given respectively by the largest eigenvalue and the corresponding eigenvector. From this decomposition, we built one easy case to illustrate the general segmentation process (all methods will succeed in this example). It is made of a spherical inclusion [figure 2] where

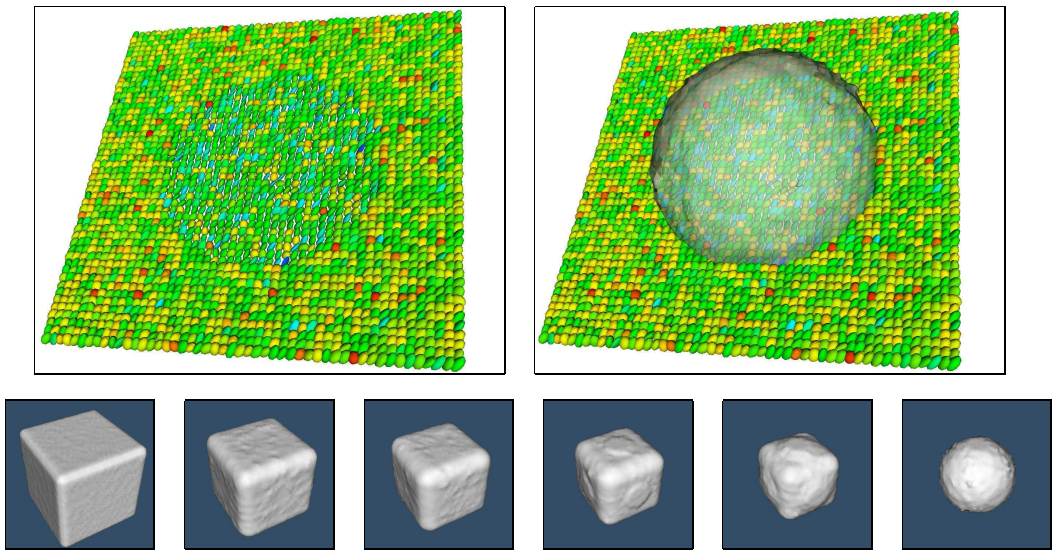

Figure 2: Segmentation (Method 1) of a noisy tensor field composed by two regions with same orientation but different scale (TOP LEFT: 2D-cut of the tensor field, TOP RIGHT: same with final segmentation, BOTTOM: surface evolution).

the difference between the inside and the outside is only based on the eigenvalues. We also generate a limit case where the two regions differ only by the major orientation of the tensors. Moreover, to make it harder, we also vary the main orientation of the tensors within the inside region by creating a junction as shown in [figure 3]. In both cases, a Gaussian noise was added directly on the eigen elements of each tensor. Initializing the surface with a bounding box, Method 1 is able to give the expected segmentations [figure 2 and 3].
However, these examples do not show the necessity of including a statistical model for the distance distribution of each region and the approach proposed in [50] for 2D fields of *pdf* gives a similar result. In order to show the advantages of our Method 2, which is more general, we have generated a second test image. This image, shown in [figure 4], is composed by one torus whose intern tensors are oriented according to the tangents of the principal circle of the torus. A noise is also added to all the tensors of the image but with a different variance whether the tensor is inside or outside the torus. In [figure 4], we compare the results obtained using [50] and our approach, for different initializations. The first method fails to segment the torus because of the orientations high variations within each region. If we initialize with a bounding box, the surface shrinks until it disappears and if we start from a small sphere inside the torus, only a small part of the torus can be captured. Using our approach 2, which models the variance of the distance between tensors, the torus is correctly extracted for the different initializations.

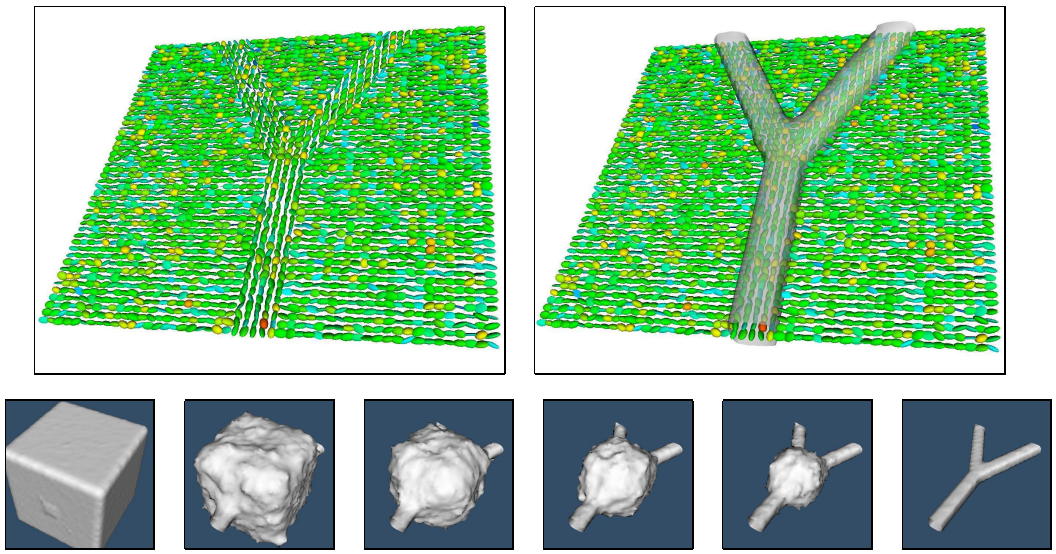

Figure 3: Segmentation (Mehtod 1) of a noisy tensor field composed by two regions with same scale but different orientations (TOP LEFT: 2D-cut of the tensor field, TOP RIGHT: same with final segmentation, BOTTOM: surface evolution).

6.2 Real DTI data

6.2.1 Experiments for Method 1 and 2

As mentioned in the introduction, the extraction of objects from DTI data is of great interest. This modality gives the opportunity to discriminate structures like the *corpus callosum* much harder to characterize using other modalities. Before any processing, we need to crop the image around the object of interest so as to respect the assumption of bi-partitioning imposed by our model. Figure 5 show the result obtained for the extraction of the *corpus callosum* with Method 1. The next experiment aims at extracting the lateral ventricles with Method 2. Two small spheres are manually placed inside the ventricles to initialize the surface. The evolution and the final segmentation are shown in [figure 6.]. This result looks really close to what we could have expected from anatomical structure extraction knowledge even though the validation for this type of data will have to be carefully addressed.

6.2.2 Improvements using the anisotropy:

When we consider the Methods 2 and 3, the initialization is really important and in many cases, several seeding points have to be set manually to avoid the surface to get stuck in a local minima. This can be overcome by introducing a global anisotropy measure. One of the most popular is based on the normalized variance of the eigenvalues: the fractional

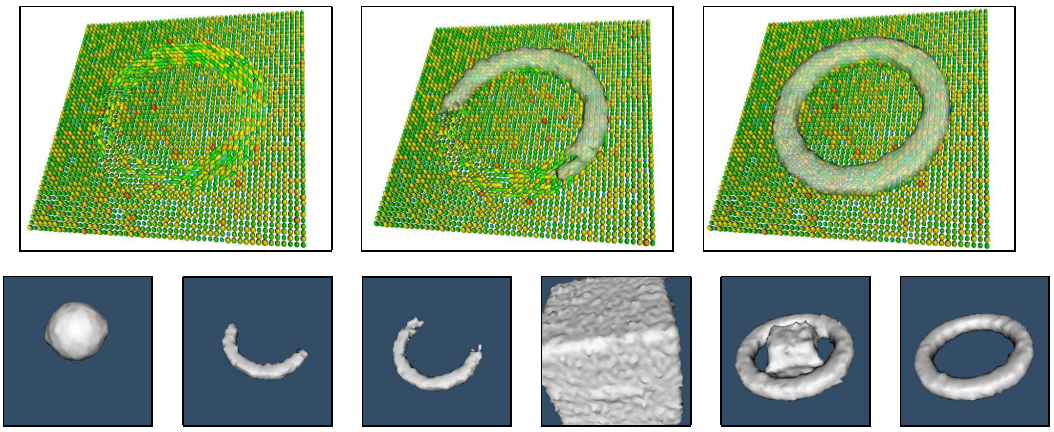

Figure 4: Segmentation of a noisy tensor field composed by two regions with different orientations (TOP LEFT: 2D-cut of the tensor field, TOP CENTER: segmentation obtained from [50], TOP RIGHT: segmentation obtained with Method 2, BOTTOM: surface evolution for both of them).

anisotropy ($\mathcal{A}$) ([4]). The advantage of this measure is that it can be computed without having to extract the tensor eigenvalues. It actually only depends on the Frobenius norm and trace of the diffusion tensor.

$$\mathcal{A}(\mathbf{D}(x)) \quad = \quad \frac{\sqrt{3}|\mathbf{D}(x) - trace(\mathbf{D}(x))\mathbf{I}/3|_F}{\sqrt{2}|\mathbf{D}(x)|_F}$$

An additional term is then defined to impose a given distribution of the anisotropy inside each region. Let $p_{a,1}$ and $p_{a,2}$ be the *pdf* of the anisotropy in Ω_1 and Ω_2, approximated by Gaussian densities. Then, according to [39] the partitioning is obtained by minimizing:

$$-\int_\Omega \big(H_\epsilon(\phi)\log p_{a,1}\mathcal{A}(\mathbf{D}(x))dx + (1-H_\epsilon(\phi))\log p_{a,2}\mathcal{A}(\mathbf{D}(x))\big)dx \tag{20}$$

This term is added to the objective function (11) defined in Section 4. Then, we obtain a new evolution equation force for the level set function ϕ composed by two terms whose influence can be controlled by adjusting the weight α between zero and one:

$$\phi_t(x) = \delta_\epsilon(\phi(x))\left(\nu \mathrm{div}\frac{\nabla\phi}{|\nabla\phi|} + (1-\alpha)\frac{1}{2}\log\frac{p_{d,2}}{p_{d,1}} + \alpha\frac{1}{2}\log\frac{p_{a,2}}{p_{a,1}}\right) \ \forall x \in \Omega \tag{21}$$

In practice, a small weight on the anisotropy term is sufficient to avoid the surface to get stuck in a local minima. For example, the extraction of the *corpus callosum* in [figure 6] was possible thanks to this additional term by setting α to 0.3. This weight should not be set too high otherwise risking to propagate to all the white matter.

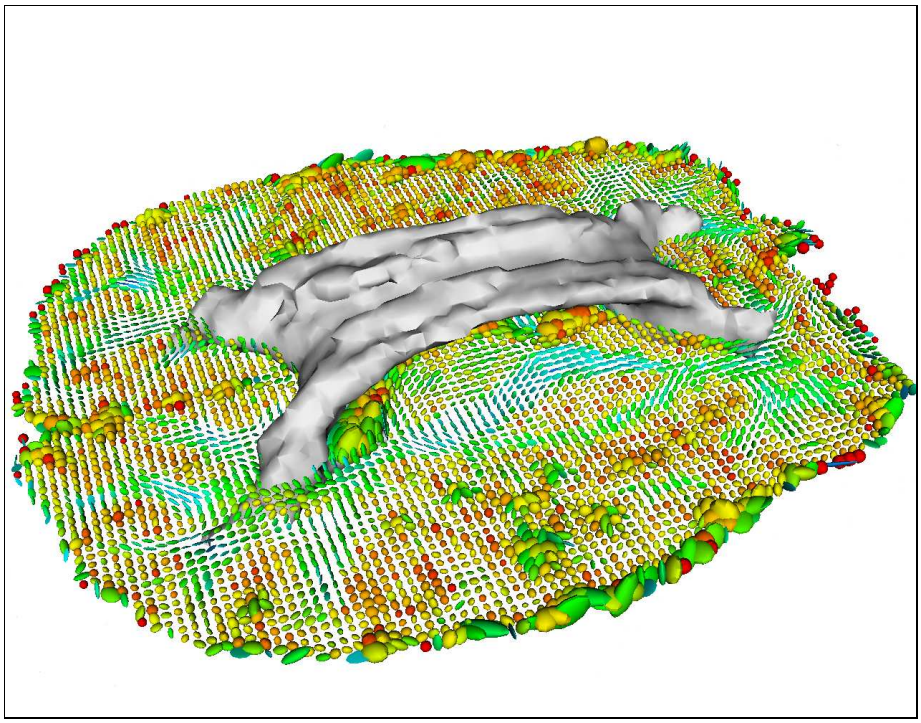

Figure 5: Segmentation of the *corpus callosum* obtained with Method 1

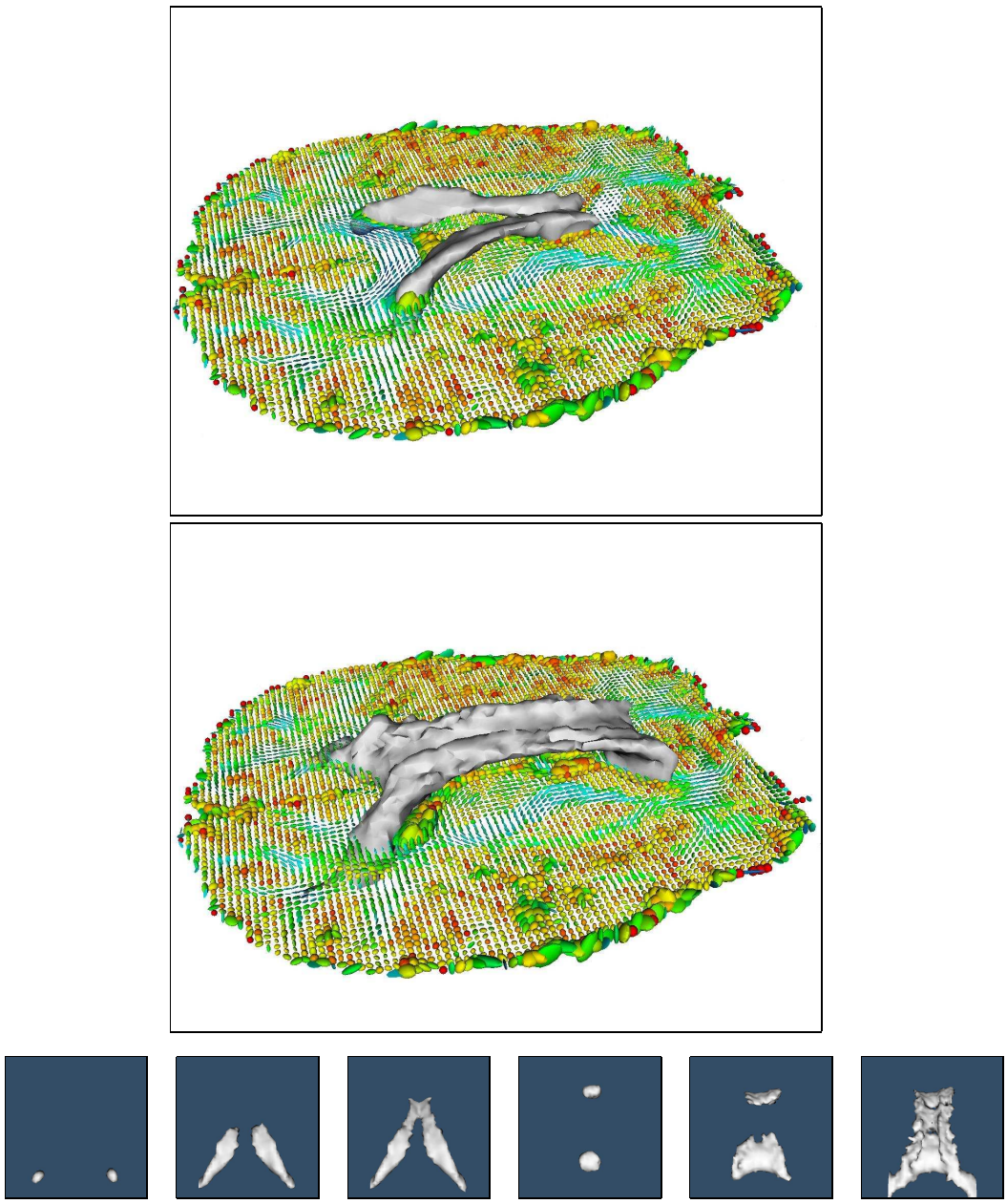

Figure 6: Segmentation of the lateral brain ventricles (TOP LEFT) and the *corpus callosum* (TOP LEFT) in a real diffusion tensor image superimposed on the DTI field using method 2, BOTTOM: surface evolution for both of them).

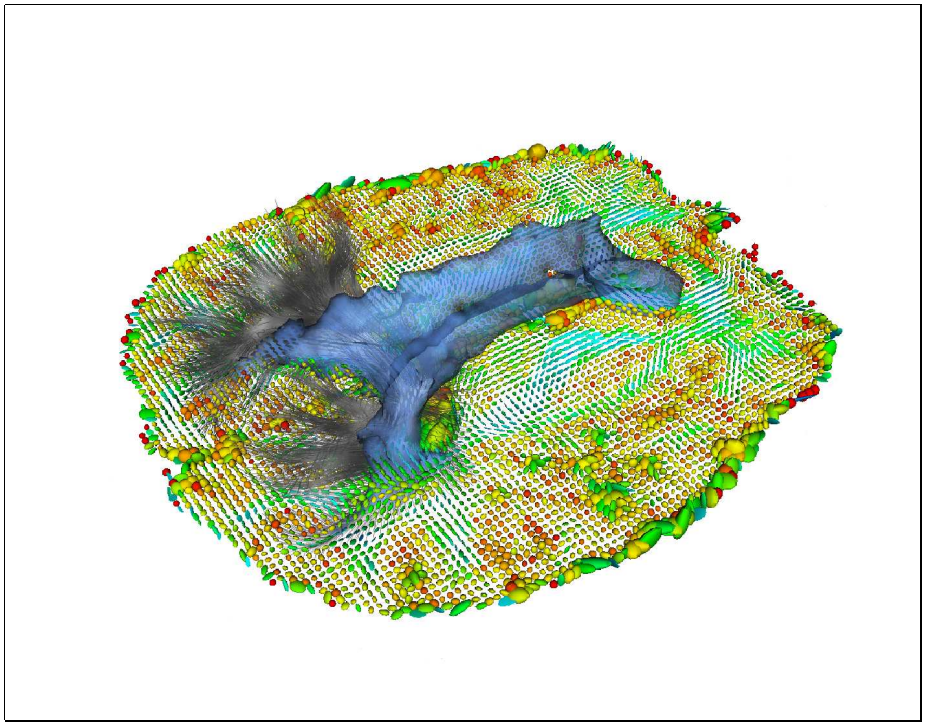

Figure 7: Segmentation by Method 2 together with callosal fibers

The comparison of figures 6 and 5 is a quite difficult task since no accurate ground-truth data is available to compare the results of Methods 1, 2 and 3. It seems that Method 1 captures more details in the *genu* whereas Method 2 and 3 may perform better in the *splenium*. The discrimination power of the methods relies on different criteria. The first method is able to capture more complex distributions by considering a full covariance matrix. The integration of such statisitical model is not straightforward for the other approaches but we are currently working on this extension and a preliminar theoretical study is presentes in [23]. To determine which one gives the desirable results will be investigated and validated with neuroanatomists.
In order to show the coherence of our results, we present on figure 7 the fusion of callosal fibers estimation by the method proposed in [21] and *corpus callosum* segmentation by Method 2 in the region of the *splenium*.

6.3 Experiments for Method 3

In order to test our Method 3, we show results on a much harder synthetic dataset on figure 8. It is composed of an helix of tensors whose orientations follow the tangent to the helix at each position. All the tensors have the same eigenvalues. While method 1 and 2 have some difficulties in capturing the whole helix, considering the natural distance helps and gives the expected results. Results on real images are presented in figure 9 for the extraction of the lateral brain ventricles and the corpus callosum. On these results, we still make use of the anisotropy term to improve the robustness. The obtained results are slightly better than when considering the Kullback-Leibler divergence but a higher statistical model for each region should be definitly considered to improve the algorithm.

7 Conclusion

We have presented three novel techniques for the segmentation of probability density fields with a major contribution to the extraction of anatomical structures in anisotropic biological tissues such as the brain white matter. We have shown that these method performs very well on synthetic data and are able to catch fine details on real DTI datasets thus exhibiting an adequate behavior of their respective segmentation criterion. We are currently working on multivariate Normal distribution over the 6-dimensional statistical manifold to model region statistics [23]. We are also in the process to compare the accuracy of the three algorithms on various sets of synthetic data.

Acknowledgments: The authors would like to thank M. Moakher (National Engineering School at Tunis, Tunisia) and K. Ugurbil, S. Lehericy, K. Lim and G. Sapiro (Center for Magnetic Resonance Research, University of Minnesota, Minneapolis, USA) and B. Vemuri, Y. Chen (University of Florida) and T. Papadopoulo for their many helpful comments and discussions regarding this work. We also gratefully acknowledge J.F. Mangin and J.B. Poline for providing us with the data used in this report.

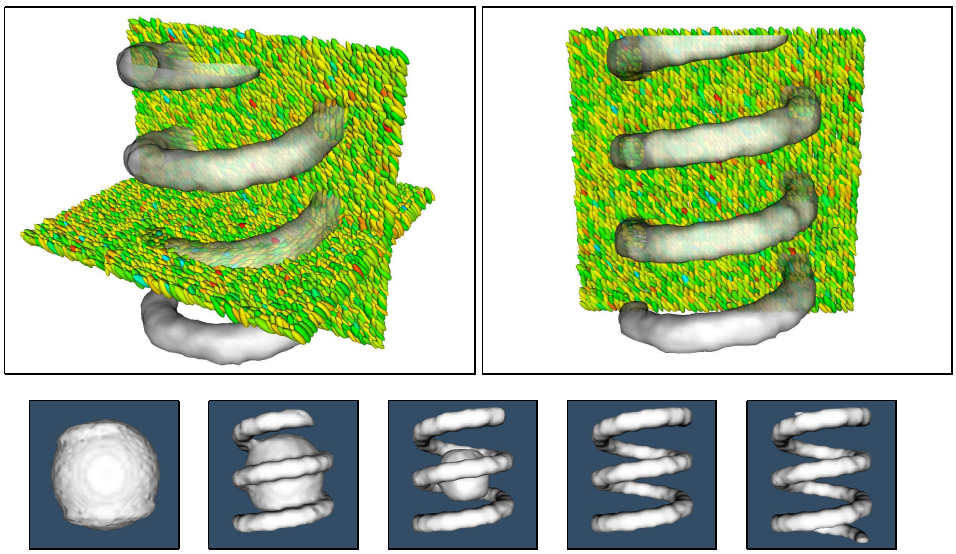

Figure 8: TOP Segmentation (Method 3) of a noisy tensor field composed by two regions with very different orientations, BOTTOM: surface evolution).

References

[1] B.A. Ardekani, J. Nierenberg, M.J. Hoptman, D.C. Javitt, and K.O. Lim. MRI study of white matter diffusion anisotropy in schizophrenia. *NeuroReport*, 14(16):2025–2029, November 2003.

[2] P.j. Basser, J. Mattiello, and D. LeBihan. MR diffusion tensor spectroscopy and imaging. *Biophysica*, (66):259–267, 1994.

[3] P.J. Basser, S. Pajevic, C. Pierpaoli, J. Duda, and A. Aldroubi. In vivo fiber tractography using DT-MRI data. *Magn. Res. Med.*, 44:625–632, 2000.

[4] P.J. Basser and C. Pierpaoli. Microstructural and physiological features of tissues elucidated by quantitative diffusion tensor MRI. *Journal of Magnetic Resonance*, 11:209–219, 1996.

[5] D. Le Bihan, E. Breton, D. Lallemand, P. Grenier, E. Cabanis, and M. Laval-Jeantet. Mr imaging of intravoxel incoherent motions: Application to diffusion and perfusion in neurologic disorders. *Radiology*, pages 401–407, 1986.

[6] M. Bjornemo, A. Brun, R. Kikinis, and C.F. Westin. Regularized stochastic white matter tractography using diffusion tensor MRI. In *MICCAI*, pages 435–442, 2002.

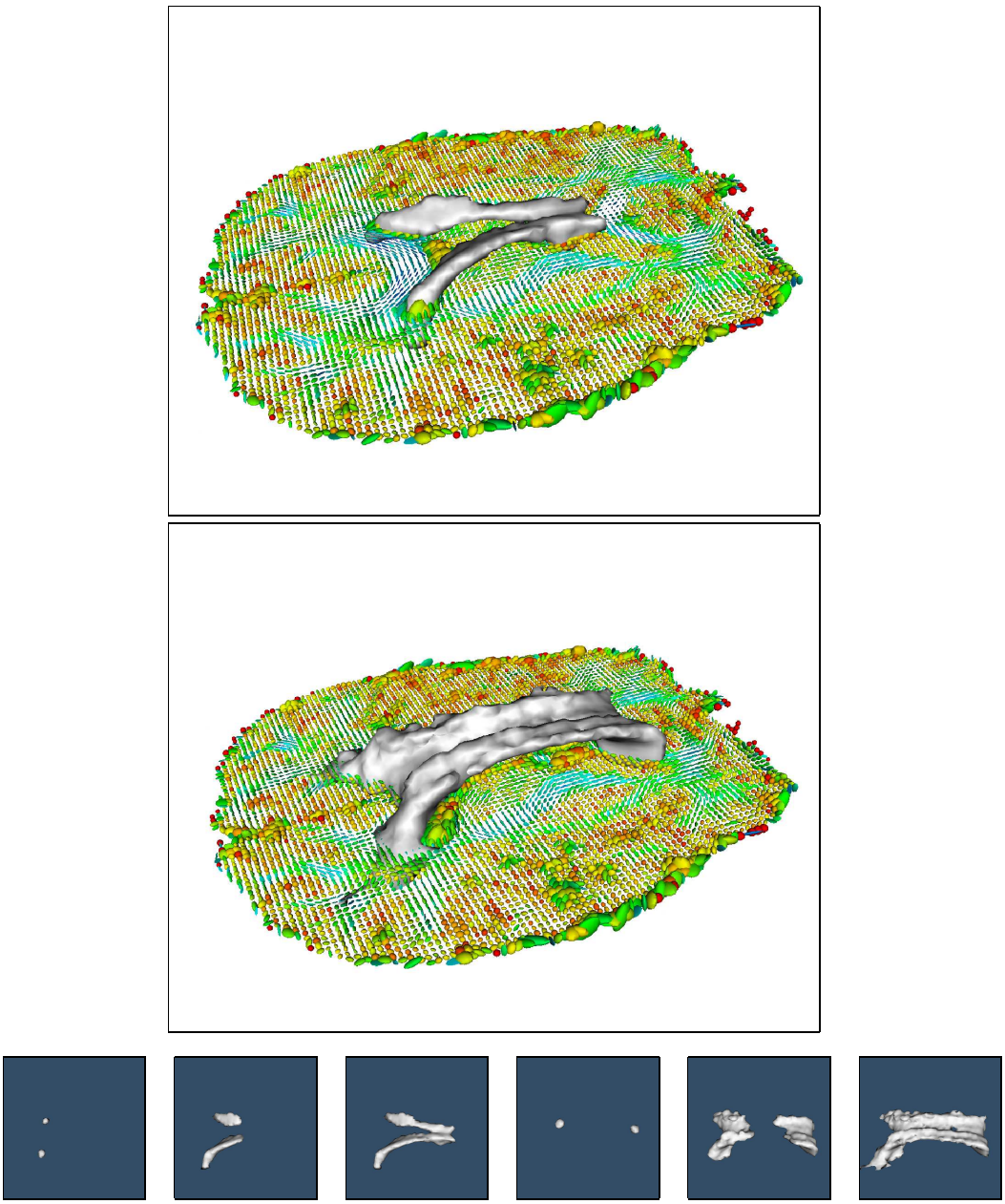

Figure 9: Segmentation of the lateral brain ventricles (TOP LEFT) and the *corpus callosum* (TOP LEFT) in a real diffusion tensor image superimposed on the DTI field using method 3, BOTTOM: surface evolution for both of them).

[7] J. Burbea. Informative geometry of probability spaces. *Expositiones Mathematica*, 4:347–378, 1986.

[8] M. Calvo and J.M. Oller. An explicit solution of information geodesic equations for the multivariate normal model. *Statistics and Decisions*, 9, 1991.

[9] J.S.W. Campbell, K. Siddiqi, B.C. Vemuri, and G.B Pike. A geometric flow for white matter fibre tract reconstruction. In *IEEE International Symposium on Biomedical Imaging Conference Proceedings*, pages 505–508, July 2002.

[10] T. Chan and L. Vese. An active contour model without edges. In *Scale-Space Theories in Computer Vision*, volume 1682 of *Lecture Notes in Computer Science*, pages 141–151. Springer–Verlag, 1999.

[11] N.N. Chentsov. Statistical decision rules and optimal inferences. In *Translations of Mathematical Monographs*. American Mathematical Society, Providence, 1982.

[12] O. Cicarelli, A.T. Toosy, G.J.M. Parker, C.A.M Wheeler-Kingshott, G.J. Barker, D.H. Miller, and A.J. Thompson. Diffusion tractography based group mapping of major white matter pathways in the human brain. *NeuroImage*, 19:1545–1555, 2003.

[13] P.S. Eriksen. Geodesics connected with the fisher metric on the multivariate manifold. Technical Report 86-13, Institute of Electronic Systems, Aalborg University, 1986.

[14] W. Förstner and B. Moonen. A metric for covariance matrices. Technical report, Stuttgart University, Dept. of Geodesy and Geoinformatics, 1999.

[15] M. Fréchet. Les éléments aléatoires de nature quelconque dans un espace distancié. *Ann. Inst. H. Poincaré*, X(IV):215–310, 1948.

[16] P. Hagmann, J.P. Thiran, L. Jonasson, P. Vandergheynst, S. Clarke, P. Maeder, and R. Meuli. Dti mapping of human brain connectivity: Statistical fiber tracking and virtual dissection. *NeuroImage*, 19:545–554, 2003.

[17] L. Jonasson, P. Hagmann, X. Bresson, R. Meuli, O. Cuisenaire, and J.P Thiran. White matter mapping in DT-MRI using geometric flows. In *EUROCAST*, pages 585–596, 2003.

[18] H. Karcher. Riemannian centre of mass and mollifier smoothing. *Comm. Pure Appl. Math*, 30:509–541, 1977.

[19] M. Lazar, D. Weinstein, K. Hasan, and A.L. Alexander. Axon tractography with tensorlines. In *Proceedings of International Society of Magnetic Resonance in Medicine*, volume 482, 2000.

[20] M. Lazar, D.M. Weinstein, J.S. Tsuruda, K.M. Hasan, K. Arfanakis, M.E. Meyerand, B. Badie, H.A. Rowley, V.Haughton, A. Field, and A.L. Alexander. White matter tractography using diffusion tensor deflection. In *Human Brain Mapping*, volume 18, pages 306–321, 2003.

[21] C. Lenglet, R. Deriche, and O. Faugeras. Inferring white matter geometry from diffusion tensor MRI: Application to connectivity mapping. In Pajdla and Matas, Prague, Czech Republic, 2004. Springer–Verlag.

[22] C. Lenglet, M. Rousson, and R. Deriche. Segmentation of 3D probability density fields by surface evolution: Application to diffusion MRI. In *Proc. 7th Intl. Conf. on Medical Image Computing and Computer Assisted Intervention*, Saint-Malo, France, September 2004.

[23] C. Lenglet, M. Rousson, R. Deriche, and O. Faugeras. Statistics on multivariate normal distributions: A geometric approach and its application to diffusion tensor MRI. Research Report 5242, INRIA, June 2004.

[24] T.E. McGraw. Neuronal fiber tracking in DT-MRI. Master's thesis, University of Florida, 2002.

[25] K.D. Merboldt, W. Hanicke, and J. Frahm. Self-diffusion nmr imaging using stimulated echoes. *J. Magn. Reson.*, 64:479–486, 1985.

[26] M. Moakher. Means and averaging in the group of rotations. *SIAM Journal on Matrix Analysis and Applications*, 24(1):1–16, 2002.

[27] M. Moakher. A differential geometric approach to the geometric mean of symmetric positive-definite matrices. *SIAM Journal on Matrix Analysis and Applications (to appear)*, 2004.

[28] S. Mori, B.J. Crain, V.P. Chacko, and P.C.M. Van Zijl. Three-dimensional tracking of axonal projections in the brain by magnetic resonance imaging. *Annals of Neurology*, 45(2):265–269, February 1999.

[29] S. Mori, B.J. Crain, and P.C. van Zijl. 3d brain fiber reconstruction from diffusion MRI. In *Proceedings of the International Conference on Functional Mapping of the Human Brain*, 1998.

[30] M.E. Moseley, Y. Cohen, J. Kucharczyk, J. Mintorovitch, H.S. Asgari, M.F. Wendland, J. Tsuruda, and D. Norman. Diffusion-weighted mr imaging of anisotropic water diffusion in cat central nervous system. *Radiology*, 176:439–445, 1999.

[31] L. O'Donnell, S. Haker, and C.F. Westin. New approaches to estimation of white matter connectivity in diffusion tensor MRI: Elliptic pdes and geodesics in a tensor-warped space. In *MICCAI*, 2002. 459–466.

[32] N. Paragios and R. Deriche. Geodesic active regions and level set methods for supervised texture segmentation. *The International Journal of Computer Vision*, 46(3):223, 2002.

[33] G.J.M. Parker. Tracing fibers tracts using fast marching. In *Proceedings of the International Society of Magnetic Resonance*, volume 85, 2000.

[34] G.J.M. Parker and D.C Alexander. Probabilistic monte carlo based mapping of cerebral connections utilising whole-brain crossing fibre information. In *IPMI*, pages 684–695, 2003.

[35] G.J.M. Parker, C.A.M. Wheeler-Kingshott, and G.J. Barker. Estimating distributed anatomical connectivity using fast marching methods and diffusion tensor imaging. *Trans. Med. Imaging*, 21(5):505–512, 2002.

[36] X. Pennec. Probabilities and statistics on riemannian manifolds: A geometric approach. Research Report 5093, INRIA, January 2004.

[37] C. Poupon. *Détection des faisceaux de fibres de la substance blanche pour l'étude de la connectivité anatomique cérébrale.* PhD thesis, Ecole Nationale Supérieure des Télécommunications, December 1999.

[38] C.R. Rao. Information and accuracy attainable in the estimation of statistical parameters. *Bull. Calcutta Math. Soc.*, 37:81–91, 1945.

[39] M. Rousson and R. Deriche. A variational framework for active and adaptative segmentation of vector valued images. In *Proc. IEEE Workshop on Motion and Video Computing*, pages 56–62, Orlando, Florida, December 2002.

[40] M. Rousson, C. Lenglet, and R. Deriche. Level set and region based surface propagation for diffusion tensor MRI segmentation. In *Computer Vision Approaches to Medical Image Analysis (CVAMIA) and Mathematical Methods in Biomedical Image Analysis (MMBIA) Workshop*, Prague, May 2004.

[41] M. Rousson, T. Brox, and R. Deriche. Active unsupervised texture segmentation on a diffusion based space. In *IEEE Conference on Computer Vision and Pattern Recognition,* pages 699–704, Madison, Wisconsin (United States), June 2003.

[42] L.T. Skovgaard. A riemannian geometry of the multivariate normal model. *Scandinavian Journal of Statistics*, 11:211–233, 1984.

[43] C. Sotak. The role of diffusion tensor imaging (dti) in the evaluation of ischemic brain injury. *NMR Biomed.*, 15:561–569, 2002.

[44] E.O. Stejskal and J.E. Tanner. Spin diffusion measurements: spin echoes in the presence of a time-dependent field gradient. *Journal of Chemical Physics*, 42:288–292, 1965.

[45] D. Tschumperlé and R. Deriche. Variational frameworks for DT-MRI estimation, regularization and visualization. In *Proceedings of the 9th International Conference on Computer Vision*, Nice, France, 2003. IEEE Computer Society, IEEE Computer Society Press.

[46] D.S. Tuch. Mapping cortical connectivity with diffusion MRI. In *ISBI*, pages 392–394, 2002.

[47] D.S. Tuch, T.G. Reese, M.R. Wiegell, and V.J. Wedeen. Diffusion MRI of complex neural architecture. *Neuron*, 40:885–895, December 2003.

[48] B. Vemuri, Y. Chen, M. Rao, T. McGraw, T. Mareci, and Z. Wang. Fiber tract mapping from diffusion tensor MRI. In *1st IEEE Workshop on Variational and Level Set Methods in Computer Vision (VLSM'01)*, July 2001.

[49] Z. Wang and B.C. Vemuri. An affine invariant tensor dissimilarity measure and its application to tensor-valued image segmentation. In *IEEE Conference on Computer Vision and Pattern Recognition*, Washington, DC., June 2004.

[50] Z. Wang and B.C. Vemuri. Tensor field segmentation using region based active contour model. In Pajdla and Matas, Prague, Czech Republic, 2004. Springer–Verlag.

[51] Z. Wang, B.C. Vemuri, Y. Chen, and T. Mareci. Simultaneous smoothing and estimation of the tensor field from diffusion tensor MRI. In *IEEE Conference on Computer Vision and Pattern Recognition,* pages 461–466, Madison, Wisconsin (United States), June 2003.

[52] D.M. Weinstein, G.L. Kindlmann, and E.C. Lundberg. Tensorlines: Advection-diffusion based propagation through tensor fields. In *IEEE Visualization*, pages 249–253, 1999.

[53] M.R. Wiegell, D.S. Tuch, H.W.B. Larson, and V.J. Wedeen. Automatic segmentation of thalamic nuclei from diffusion tensor magnetic resonance imaging. *NeuroImage*, 19:391–402, 2003.

[54] Y. Zhang, M. Brady, and S. Smith. Segmentation of brain MR images through a hidden markov random field model and the expectation-maximization algorithm. *IEEE Transactions on Medical Imaging*, 20(1), January 2001.

[55] L. Zhukov and A.H. Barr. Oriented tensor reconstruction: Tracing neural pathways from diffusion tensor MRI. In *Proceedings of the conference on Visualization '02*, pages 387–394, 2002.

[56] L. Zhukov, K. Museth, D. Breen, R. Whitaker, and A.H. Barr. Level set segmentation and modeling of DT-MRI human brain data. *Journal of Electronic Imaging*, 2003.

Unité de recherche INRIA Sophia Antipolis
2004, route des Lucioles - BP 93 - 06902 Sophia Antipolis Cedex (France)

Unité de recherche INRIA Futurs : Parc Club Orsay Université - ZAC des Vignes
4, rue Jacques Monod - 91893 ORSAY Cedex (France)
Unité de recherche INRIA Lorraine : LORIA, Technopôle de Nancy-Brabois - Campus scientifique
615, rue du Jardin Botanique - BP 101 - 54602 Villers-lès-Nancy Cedex (France)
Unité de recherche INRIA Rennes : IRISA, Campus universitaire de Beaulieu - 35042 Rennes Cedex (France)
Unité de recherche INRIA Rhône-Alpes : 655, avenue de l'Europe - 38334 Montbonnot Saint-Ismier (France)
Unité de recherche INRIA Rocquencourt : Domaine de Voluceau - Rocquencourt - BP 105 - 78153 Le Chesnay Cedex (France)

Éditeur
INRIA - Domaine de Voluceau - Rocquencourt, BP 105 - 78153 Le Chesnay Cedex (France)
http://www.inria.fr
ISSN 0249-6399